Anthrax Toxin Translocation Complex Reveals insight into the Lethal Factor Unfolding and Refolding Mechanism

Alexandra J Machen[1], Mark T Fisher*[1], Bret D Freudenthal*[1]

1 [1]Department of Biochemistry and Molecular Biology, University of Kansas Medical Center,

2 Kansas City, KS 66160, USA.

3 *Co-corresponding Authors. Correspondence to bfreudenthal@kumc.edu

Abstract

Translocation is essential to the anthrax toxin mechanism. Protective antigen (PA), the translocon component of this AB toxin, forms an oligomeric pore with three key clamp sites that aid in the efficient entry of lethal factor (LF) or edema factor (EF), the enzymatic components of the toxin, into the cell. LF and EF translocate through the PA pore (PA_{pore}) with the pH gradient between the endosome and the cytosol facilitating rapid translocation *in vivo*. Structural details of the translocation process have remained elusive despite their biological importance. To overcome the technical challenges of studying translocation intermediates, we developed a novel method to immobilize, transition, and stabilize anthrax toxin to mimic important physiological steps in the intoxication process. Here, we report a cryoEM snapshot of PA_{pore} translocating the N-terminal domain of LF (LF_N). The resulting 3.3 Å structure of the complex shows density of partially unfolded LF_N near the canonical PA_{pore} binding site as well as in the α clamp, the Φ clamp, and the charge clamp. We also observe density consistent with an α helix emerging from the 100 Å β barrel channel suggesting LF secondary structural elements begin to refold in the pore channel. We conclude the anthrax toxin β barrel aids in efficient folding of its enzymatic payload prior to channel exit. Our hypothesized refolding mechanism has broader implications for pore length of other protein translocating toxins.

Keywords: Translocation, Anthrax, CryoEM, Refolding

22 **Significance Statement**

23 Toxins like the anthrax toxin aid bacteria in establishing an infection, evading the immune system,
24 and proliferating inside a host. The anthrax toxin, a proteinaceous AB toxin secreted by *Bacillus*
25 *anthracis,* consists of lethal factor and protective antigen. In this work, we explore the molecular
26 details of lethal factor translocation through protective antigen pore necessary for cellular entry.
27 Our cryo electron microscopy results provide evidence of lethal factor secondary structure
28 refolding prior to protective antigen pore exit. Similar to the ribosome exit tunnel, the toxin pore
29 channel likely contributes to native folding of lethal factor. We predict other AB toxins with
30 extended pores also initiate substrate refolding inside the translocon for effective intoxication
31 during bacterial infection, evasion, and proliferation.

32 **Introduction**

33 The anthrax toxin is not only a deadly *Bacillus anthracis* virulence factor, but also serves
34 as a model system of protein translocation and as a peptide therapeutic delivery platform (1, 2).
35 It's biological importance and biotechnology utility have spurred significant biochemical and
36 biophysical advances in understanding the anthrax intoxication mechanism. In order to gain entry
37 into the cell, this archetypical AB toxin must cross the endosomal membrane. Membrane
38 penetration is accomplished by the B component of anthrax toxin, termed protective antigen (PA).
39 PA forms a translocon pore through which lethal factor (LF) or edema factor (EF), the A
40 component, translocate. Here, we developed an approach to elucidate the structural and
41 mechanistic details of the anthrax toxin during translocation in an effort to understand how LF
42 unfolds in the endosome, translocates through PA, and refolds in the cytosol.

43 An overview of the anthrax toxin mechanism has been reviewed by the Collier lab (1) and
44 is briefly summarized here. The first step in intoxication is the 85 kDa monomeric PA binding to
45 host cell receptors. Then the pro-domain of PA is cleaved leaving the 63 kDa PA to oligomerize
46 into heptameric or octameric prepore ($PA_{prepore}$) (3, 4). Up to three LF and/or EF components can
47 bind to the $PA_{prepore}$ heptamer (4-6). The AB toxin complex is endocytosed through clathrin
48 mediated endocytosis (7). As the endosome acidifies, $PA_{prepore}$ undergoes a conformational
49 change to a pore (PA_{pore}) (8). This pore inserts into the endosomal membrane to form a channel.
50 The low pH of the endosome and the pH gradient between the endosome and the cytosol facilitate
51 LF or EF to unfold and rapidly translocate into the cytosol in a hypothesized Brownian ratchet
52 mechanism (9). Natively refolded LF and EF in the cytosol are then able to perform their virulent
53 enzymatic functions (10).

54 The overall structure of the PA_{pore} translocon can be divided into two regions: the funnel
55 and the channel (**Fig. 1A**). The first region, the funnel, facilitates binding and unfolding of LF. LF
56 binds to the rim of the PA_{pore} funnel and is guided down the narrowing structure. The second
57 region of PA_{pore} is the channel, a β barrel that extends from the funnel and spans the endosomal

58 membrane. Three nonspecific PA_{pore} clamp sites (α, Φ, and charge clamp) aid in the translocation
59 of LF (**Fig. 1A**). The α clamp is located at the PA funnel rim, is formed by adjacent PA protomers,
60 and binds helical portions of LF to position them towards the pore lumen. Heptameric PA_{pore} has
61 seven potential α clamp binding sites. A crystal structure of the N-terminal domain of LF (LF_N)
62 bound to the $PA_{prepore}$ revealed the α clamp binding site, but was unable to resolve the 28 amino
63 acids of LF_N passed the α clamp (11). The second clamp site is the Φ clamp, a ring of seven
64 phenylalanine residues that maintain the pH gradient between the endosome and the cytosol (12).
65 The cryoEM structure of apo PA_{pore} revealed the Φ clamp forms a narrow 6 Å diameter ring (13).
66 Secondary structural elements, such as α helices, are too wide to fit through this narrow seal.
67 Therefore, it is hypothesized that peptide substrates must completely unfold and refold in order
68 to translocate through the PA_{pore} and enter the cytosol of the cell (13). The Φ clamp also assists
69 in the unfolding of LF as an unfolding chaperone (2). The third clamp site, the charge clamp, is
70 located within the β barrel of PA_{pore}. The charge clamp deprotonates acidic side chains of LF and
71 ensures unidirectional movement of the polypeptide (14, 15). Interestingly, the diameter of the
72 PA_{pore} β barrel is large enough to accomidate an α helix, which would allow for initial refolding to
73 occur inside the pore prior to LF entering the cytosol. However, it remains unclear what structural
74 state LF is in when interacting with the charge clamp and within the β barrel channel.
75 One of the many challenges in studying the anthrax toxin is that it is a dynamic membrane
76 protein that functions under acidic conditions. Thus many questions remain, such as what path
77 LF travels down the endosomal pore lumen from the α clamp to the Φ clamp, whether the Φ clamp
78 adopts multiple states during translocation, and whether LF can partially refold inside the β barrel
79 pore. To address these questions, we developed a novel toxin immobilization, translocation, and
80 nanodisc stabilization (TITaNS) method in combination with cryoEM to structurally characterize
81 PA_{pore} translocating the N-terminal domain of LF (LF_N). This approach provides unique
82 mechanistic insight into how LF_N interacts with the three clamp sites of PA_{pore}. We observed

83 density consistent with LF_N unfolding prior to the α clamp, translocating through the dynamic Φ
84 clamp, and beginning to refold in the channel of the PA_{pore}.
85
86 **Results**
87 *Assembly of Anthrax Translocation Complexes*
88 *In vivo*, the anthrax toxin undergoes a prepore to pore conformational change under acidic
89 conditions. Previous approaches have generally used urea to avoid aggregation during the
90 transition from $PA_{prepore}$ to PA_{pore} (16-21). These approaches have limitations in that they do not
91 account for the low pH electrostatic microenvironment in the pore lumen predicted to be important
92 for LF-PA interactions (22) and they assume similar outcomes for chaotrope and acid induced
93 unfolding. In order to overcome these limitations we have developed a novel assembly method
94 for toxin immobilization, translocation, and nanodisc stabilization (called TITaNS, **Fig. 1B-G**).
95 TITaNS was designed to mimic important low pH physiological states during the anthrax
96 intoxication mechanism. This approach allows for endosomal pH pore formation and imaging of
97 individual complexes in a lipid bilayer in the biologically relevant low pH environment (16, 23).
98 TITaNS can be used in combination with techniques other than cryoEM, including mass
99 spectrometry, nuclear magnetic resonance, surface plasmon resonance, and biolayer
100 interferometry. TITaNS also has the potential to be adapted to screen prospective
101 pharmaceuticals that arrest or prevent endosomal membrane insertion (23).
102 Reversible immobilization is key to the TITaNS methodology, because it allows the
103 stabilized complexes to be released into solution. We began with recombinantly purified, soluble
104 forms of LF_N and $PA_{prepore}$ that are mixed together in solution. The binary complex of LF_N bound
105 to $PA_{prepore}$ was then immobilized onto thiol sepharose beads by covalently coupling E126C LF_N
106 to the bead surface (**Fig. 1B**). The immobilized LF_N-$PA_{prepore}$ complex was oriented such that when
107 the bead slurry was washed in pH 5.5 buffer to transition PA from prepore to pore, the pore
108 extended away from the bead surface (**Fig. 1C**). We predict this low pH environment initiates

109 translocation of LF_N through PA_{pore} *in vitro* (**Fig. 1D**). We base this prediction on computational
110 and experimental evidence of early translocation events induced by low pH. Specifically,
111 molecular simulations of anthrax toxin early translocation events predict the events are strongly
112 influenced by the protonation state of LF and are highly favorable at low pH (22). Also at low pH,
113 the partial translocation of LF has been observed in planar lipid bilayers (9). After pore formation,
114 the next step in TITaNS was the stabilization of LF_N-PA_{pore} translocation complexes using
115 nanodisc technology (24-26). Pre-nanodisc micelles were added to the bead slurry and
116 associated with the transmembrane portion of PA_{pore} (**Fig. 1E**). To promote lipid bilayer formation,
117 we dialyzed away excess detergent (**Fig. 1F**). The soluble LF_N-PA_{pore}-nanodisc complexes were
118 then eluted off the thiol sepharose beads using the reducing agent dithiothreitol. Eluted complexes
119 were transferred to the cryoEM grid and the pH was dropped to pH 5.5 to capture the complex at
120 low pH prior to blotting and plunge freezing (**Fig. 1G**). To prevent aggregation and migration of
121 the nanodiscs to the air-water interface, we plunge froze the grids within 30 seconds of sample
122 application. Using our TITaNS methodology, we obtained a 3.3 Å reconstruction of LF_N
123 translocating through PA_{pore} (**Fig. 2A-D)**.
124
125 *Comparison of LF_N before and during Translocation*
126 Prior to translocation, LF_N is bound to the cap of PA at the interface of two PA protomers
127 with helix α1 bound to the α clamp (11, 17). Our reconstruction shows a loss of LF_N density in the
128 canonical binding site above the PA_{pore} (**Fig. 2A,B**). Lethal factor translocates through PA_{pore} from
129 the N-terminus to the C-terminus. Notably, our reconstruction does not show density for residues
130 50-135 in the canonical folded LF_N position (**Fig. 2B,D)** (11, 16). However, density for residues
131 136-250 are apparent. Our model of unfolding, translocating LF_N is consistent with a molten
132 globular intermediate state at low pH (27). In our translocating LF_N complex, immobilized residue
133 E126C has not yet translocated suggesting translocation occurred while the residue was coupled
134 to the bead surface at pH 5.5, stalling the complex at this position (**Fig. 2C,D**).

135

136 *Molecular Interactions of Translocation Complex*

137 In addition to a loss of LF_N density in the canonical binding site above the PA_{pore}, our
138 reconstruction shows added density inside the pore lumen indicating a translocating complex
139 **(Fig. 3).** Density near the top of the PA_{pore} funnel was in proximity to several hydrophobic residues
140 of PA_{pore} (**Fig. 3B**). Some of these residues, including Phe202, Phe236 and Phe464 are in the α
141 clamp and have previously been proposed to aid in unfolding LF and stabilizing unfolded
142 intermediates as they transition into the pore (11). Additional hydrophobic residues further down
143 the pore lumen, such as Trp226 and Tyr456 may also help to stabilize the unfolded peptide. Our
144 results are consistent with these hydrophobic residues facilitating translocation of LF_N into the
145 pore and toward the Φ clamp in an unfolded state. We observed added asymmetric density in
146 and around the Φ clamp (**Fig. 3C**) that was not visible when we compared it to the previously
147 published apo PA_{pore} cryoEM structure (13). Specifically, there is density in the center of the Φ
148 clamp (**Fig. 3C**). We attribute this density to unfolded LF_N interacting with the Phe ring of the
149 PA_{pore} Φ clamp loops as LF_N is translocating through the pore. In addition the density for each of
150 the PA_{pore} Phe427 residues was smeared in plane with the benzyl ring suggesting rotameric states
151 moving up and down (**Fig. 3D)**.

152 Translocating LF_N density was also observed in the β barrel of the PA_{pore}. Focused
153 refinement of the β barrel interior revealed density consistent with α helices along with portions of
154 unfolded peptide (**Fig. 3E-G)**. Notably, density located at the PA_{pore} charge clamp is consistent
155 with an α helix and suggests the deprotonated state of LF favors helix formation within the pore.
156 Canonical charge clamp residues Asp276, Glu343, and Asp335 are shown in **Fig. 3E** with the
157 predicted LF_N density translocating through the center of the channel. Further down the pore we
158 observe density for helix α1 emerging from the channel exit **(Fig. 3F,G).** Our results provide
159 evidence for initial refolding of LF secondary structure both inside and upon exit from the PA_{pore}.
160 These results are consistent with ribosome exit tunnel studies that, using optical tweezers and

161 molecular dynamics simulations, showed excluded volume effects and electrostatic interactions
162 contribute to substrate folding (28).

163 Next, we wanted to determine whether there were any differences between PA_{pore}
164 protomers that interacted directly with the translocating LF_N compared to protomers that did not
165 interact with translocating LF_N. Importantly, symmetry operations were not used during single
166 particle analysis. To compare the PA_{pore} protomers, we aligned the seven protomer chains that
167 compose the PA_{pore} **(Fig. S1A)**. Comparison of the chains showed little difference in the backbone
168 or side chain rotamers for the majority of the residues at the LF_N-PA_{pore} interfaces as well as the
169 protomer-protomer interfaces. This rigidity is likely necessary for the PA_{pore} to maintain a stable β
170 barrel and perform its function under endosomal conditions. During this analysis, we also
171 examined the conformation of the receptor binding domain of PA_{pore}. The receptor binding domain
172 is connected to the main body of PA_{pore} by a single loop and is responsible for anchoring the toxin
173 to the host cell membrane prior to complex endocytosis and pore formation (29). Interestingly, the
174 receptor binding domain did show different conformations for each protomer and indicates a
175 degree of conformational flexibility **(Fig. S1A-C)**. This variability between receptor binding
176 domains likely arose from the acidic conditions and lack of a receptor. Overlaying our PA_{pore}
177 chains with the crystal structure of $PA_{prepore}$ bound to its receptor, capillary morphogenesis protein
178 2 (CMG2), revealed several conformations not conducive to receptor binding **(Fig. S1C)**.
179 Specifically, PA E194 was not in position to form the metal ion-dependent adhesion site (MIDAS)
180 motif in the receptor binding pocket (30). This indicates that without a receptor bound, the receptor
181 binding domain loops adopt multiple states.

182

183 **Discussion**

184 The anthrax toxin PA_{pore} unfolds, translocates, and refolds LF, it's enzymatic subtrate.
185 Three clamp sites aid in peptide translocation: the α clamp, the Φ clamp, and the charge clamp.
186 We report here, cryoEM density consistent with nascent polypeptide chain translocating the length

187 of PA_{pore}. In our model, LF_N can be seen unfolding prior to the α clamp, passing through the
188 dynamic Φ clamp, and refolding in the β barrel channel. This model is consistent with LF needing
189 to completely unfold in order to translocate. However, if the entire 90 kDa enzyme were to unfold
190 at once, deleterious folded intermediates or aggregates would likely block the PA_{pore} translocon,
191 especially when multiple LF are bound to PA. Therefore, in order to efficiently translocate and
192 refold, LF unfolds from the N to C terminus (31). While the low pH of the endosome destabilizes
193 the enzyme, it does not completely unfold into its primary sequence (27, 32). Our results are
194 consistent with molten globular translocation intermediates of LF being destabilized in the acidic
195 environment of the endosome (27) with the α clamp then able to apply additional unfolding force
196 on the protein and funnel LF towards the Φ clamp (2). Translocation requires step-wise unfolding
197 and stabilization of the unfolded intermediates to prevent aggregation. When LF binds to PA_{pore},
198 helix α1 of LF moves away from the main body of LF and binds to the α clamp of PA_{pore} (11). From
199 here, LF has multiple paths it could take through the PA_{pore} funnel, gated by the Φ clamp. Our
200 results suggest a favorable path from the α to Φ clamp that involves a series of hydrophobic
201 residues that are amenable to unfolded translocation intermediates and likely serve as
202 checkpoints to verify the unfolded state of LF prior to the Φ clamp (**Fig. 3A-B)**.

203 The Φ clamp plays a crucial roll in translocation by acting as a hydrophobic seal between
204 the endosome and cytosol (9). Multiple Φ clamp states have been hypothesized at pH 5.5 (33).
205 Our analysis did not reveal multiple distinct states. However, the smeared density in our structure
206 is indicative of a dynamic clamp. Our density does not imply dilation of the clamp (33), so much
207 as a up and down motion along the pore axis. This motion could be conserted or individual F427
208 residues moving to accommodate various translocating side chains. The compressive and tensile
209 forces generated by the unfolding LF in the PA_{pore} funnel above and the refolding LF in the β barrel
210 channel below may also contribute to this movement. However, too much flexibility or dialation
211 would cause the seal at the Φ clamp to be lost. Therefore, this dynamic motion must still maintain

212 the pH gradient between the endosome and cytosol, while accomidating any side chain, ensuring
213 efficient translocation.

214 Helix formation inside the PA_{pore} β barrel has been hypothesized but, to our knowledge,
215 never observed (13, 27). We report here, evidence of concomitant α helix formation and
216 translocation inside the β barrel of the PA_{pore} (**Fig. 3E,F,G)**. We hypothesized that, along with
217 changing the charge state of the peptide substrate, the charge clamp allows for a local folding
218 environment within the PA_{pore}. Helical portions of LF have previously been shown to dock into the
219 α clamp, with the periodicity of these helices aiding in efficient unfolding of LF (34). We predict
220 this periodicity is also important for hypothesized refolding of LF, beginning at the charge clamp.
221 Our hypothesis is consistent with other anthrax toxin subtrates, such as LF_N fused to the catalytic
222 chain of diphtheria toxin (LF_N-DTA), which did not evolve to fold in the PA_{pore} channel.
223 Interestingly, these non-native substrates require chaperones for enzymatic activity (35)
224 indicating the DTA portion of these proteins do not form helices in the PA channel at optimal
225 intervals. Our model is also reminesant of the ribosome, where helix folding in the exit tunnel aids
226 in co-translational folding of native proteins (36). We predict helix folding in the PA_{pore} β barrel
227 aids in co-translocational folding by temporally altering LF emersion from the tunnel allowing
228 regions to fold into tertiary structures.

229 A proposed unfolding-refolding translocation model is shown in **Fig. 4A** starting with LF_N
230 bound to the funnel rim of $PA_{pore.}$ LF_N is unfolded and funnelled towards the Φ clamp, aided by
231 hydrophobic residues along the funnel slope. LF_N acidic residues are protonated in the acidic
232 environment of the funnel. Completely unfolded LF_N then passes the Φ clamp. This ring of F427
233 residues remains restrictive enough to maintain a seal while accomdating translocation. As the
234 channel widens in the charge clamp, acidic residues are deprotonated. Folding of α helical
235 portions places mechanical force on the translocating peptide, contributing to efficient
236 translocation, and overcoming local energy minimum that could otherwise stall the complex. The

237 newly formed, secondary structure favors unidirectional translocation by discouraging retrograde
238 transfer through the narrow Φ clamp resulting in natively folded LF in the host cell cytosol.
239 Our results have implications for other toxins. PA Phe427 is equivalent to Phe454 of
240 *Clostridium perfringens* iota toxin (37), Phe428 of *Clostridium botulinum* C2II binary toxin (38),
241 and Trp318 of *Vibrio cholerae* cytolysin (39). We hypothesize a dynamic hydrophobic seal model
242 is a common mechanism, applicable to these other toxins. Initial refolding in the pore channel is
243 also likely not unique to the anthrax toxin. Indeed, other translocons, such as the iota toxin and
244 toxin complex (Tc) toxin (**Fig. 4B**), have pores that extend well passed the membrane bilayer (40,
245 41). We predict these pore forming toxins have evolved extended pores to faciliate substrate
246 refolding inside the translocon for effective intoxication. Not all pore forming toxins translocate
247 proteins. Some, like *Vibrio cholerae* cytolysin (VCC) and *Staphylococcus aureus* α-hemolysin,
248 form pores to distrupt ion concentrations (39, 42). The pore length of these toxins is noticeably
249 shorter (**Fig. 4B**).
250
251 **Materials and Methods**
252 *Protein Expression and Purification*
253 Proteins were purified as previously described (16). Briefly, His_6-SUMO-LF_N E126C was
254 expressed in BL21 cells, purified using anion exchange, and cleaved by small ubiquitin-related
255 modifier protease (43). Recombinant wild-type PA_{83} was expressed in the periplasm
256 of *Escherichia coli* BL21 (DE3) and purified by ammonium precipitation and anion exchange
257 chromatography (8). After trypsin activation (43), PA_{63} heptameric prepores were formed using
258 anion exchange and size exclusion chromatography. Membrane scaffold protein 1D1 (MSP1D1)
259 was expressed from the pMSP1D1 plasmid (AddGene) with an N-terminal His-tag and was
260 purified by affinity chromatography (26).
261
262 *LF_N-PA-Nanodisc Complex Formation for CryoEM with TITaNS*

263 E126C LF_N and $PA_{prepore}$ were incubated in solution and then immobilized by coupling
264 E126C LF_N to activated thiol sepharose 4B beads (GE Healthcare Bio-Sciences, Pittsburgh, PA,
265 USA) in Assembly Buffer (50 mM Tris, 50 mM NaCl, 10mM $CaCl_2$ pH 7.5) at 4 °C for 12 hr. Beads
266 were washed three times with Assembly Buffer to remove any unbound $PA_{prepore}$. The immobilized
267 LF_N-$PA_{prepore}$ complexes were then incubated in low pH buffer (10 mM acetate, 50 mM Tris, 50
268 mM NaCl, 10mM $CaCl_2$ pH 5.5) to transition the $PA_{prepore}$ to PA_{pore} and initiate translocation of LF_N.
269 The beads were then washed in Assembly Buffer at neutral pH three times. Next, pre-nanodisc
270 micelles (2.5 μM MSP1D1, 97.5 μM 1-palmitoyl-2-oleoyl-sn-glycero-3-phosphocholine (POPC)
271 (Avanti, Alabaster, AL, USA), 65 (POPG) in 25 mM Na-cholate (Sigma-Aldrich, St. Louis, MO,
272 USA), 50 mM Tris, and 50 mM NaCl) were added and bound to the aggregation-prone
273 hydrophobic transmembrane β-barrel of PA_{pore}. The micelles were collapsed into nanodiscs by
274 removing Na-cholate using dialysis with Bio-Beads (BIO RAD, Hercules, CA, USA). Stabilized
275 complexes were released from the thiol sepharose beads by reducing the E126C LF_N-bead
276 disulfide bond using 50 mM dithiothreitol (DTT) (Goldbio, St. Louis, MO, USA) in Assembly Buffer.
277 Assembled complexes were initially confirmed using negative-stain TEM. Complexes were stored
278 at -80C prior to cryoEM grid preparation. Complex formation has also previously been confirmed
279 using mass spectrometry and biolayer interferometry (44).
280
281 *Grid Preparation for CryoEM*
282 Complexes stored at -80C were thawed on ice. A glow discharged Quantifoil R1.2/1.3
283 300M Cu holey carbon grid was placed inside the FEI Vitrobot Mark IV humidity chamber at
284 100% humidity. Then, 2ul of thawed sample was applied to the grid followed by 0.5uL of 1M
285 acetate pH 5.5. The grids were then blotted and plunge frozen in liquid ethane. Frozen grids
286 were stored in liquid nitrogen prior to use.
287
288 *CryoEM Data Collection and Image Processing*

CryoEM grids were loaded into a FEI Titan Krios electron microscope operated at 300 kV for automated image acquisition with serialEM (45). cryoEM micrographs were recorded as movies on a Gatan K2 Summit direct electron detection camera using the electron counting mode in super resolution mode at ×130K nominal magnification, a pixel size of 0.535 Å per pixel, and defocus ranging between −1 and −3 μm. Total dose was 50.76 e-/ $Å^2$. Total exposure time was 9s and fractionated into 45 frames with 200 ms exposure time for each frame. In total, 6,515 micrographs were taken in a continuous session. Frames in each movie were aligned and averaged for correction of beam-induced drift using MotionCor2 and cryoSPARC patch motion correction to generate a micrograph (46, 47). Micrographs generated by averaging all frames of each movie were used for defocus determination and particle picking. Micrographs obtained by averaging frames 2-36 (corresponding to ~40 e/$Å^2$) were used for two- and three-dimensional image classifications. The best 4,488 micrographs were selected for the following in-depth data processing.

Single Particle Analysis and Density Modification

Single particle analysis was performed using cryoSPARC v2.15 (46) **(Fig. S2)**. A random subset of micrographs was selected for blob particle picking. These particles were subjected to 2D classification in order to obtain a set of five particle templates. Using these templates, 2,076,581 particles were selected from 4,488 micrographs. After multiple rounds of 2D classification, the remaining 671,090 'good' particles were used to create an *ab initio* model. Heterogenous classification with four classes was then performed and the class with full length β barrel and nanodisc was selected. To select particles with LF_N, 3D variability analysis was performed with three orthogonal principle modes (i.e. eigenvectors of 3D covariance) and a mask of LF_N bound in each of the seven possible binding sites filtered to 30 Å and gaussian blurred. 122,651 particles from three resulting clusters with potential LF_N density were selected for further processing. A non-uniform refinement on the per particle motion and CTF corrected particles was

315 performed resulting in a 3.3 Å cryoEM density map. Resolution was determined using gold
316 standard Fourier shell correlation with a cut off of 0.143. Next, local refinements and density
317 modifications were performed (**Fig. S3**). To further characterize bound $LF_{N,}$ local refinement of
318 the cap of the PA_{pore} was performed using a mask of LF_N (PDB 3KWV) low pass filtered to 30 Å.
319 For the β barrel interior, a cylindrical mask was used. Phenix density modification was perfomed
320 on the non-uniform refinement and local refinement half maps to further improve the density for
321 PA_{pore} and LF_N, respectively (48). Phenix combined focused maps was then used to create a
322 composite map (**Fig. S3**) (49). The map showed density surrounding the transmembrane region
323 of the beta barrel that we interpret as nanodisc density. As has been reported previously (13),
324 there was also disordered density surrounding the outside of the middle of the β barrel. This
325 additional density was masked out of the final map using a 30 Å mask of LF_N-PA_{pore} inserted into
326 a nanodisc.
327
328 *Model Building and Refinement*
329 An initial model using PDB 6PSN was docked into the cryoEM map using Chimera map
330 to model (50). The LF_N coarse model was adjusted manually using Coot (51) to fit the density
331 starting at the C-terminus. Model α helical assignments were based on helicity in original
332 model, cryoEM density diameter, and consistency with previously published helical density.
333 The PA_{pore} coarse model was refined using PHENIX real space refine (49). Individual atomic
334 model side chains were manually adjusted to fit the density map using Coot (51). This process
335 was repeated iteratively until an optimal model was obtained. Ramachandran plots and
336 MolProbity (52) were used to assess model quality. **Supplementary Table 1** is a summary of
337 cryoEM data collection and processing as well as model building and validation.
338
339 **Acknowledgements**

This work is dedicated to the memory of our friend, mentor, and colleague Dr. Mark T. Fisher. This work was supported by National Institutes of Health (R35-GM128562 and R03-AI142361 to B.D.F.), and by University of Kansas Madison and Lila Self Graduate Fellowship to A.J.M. The authors acknowledge the use of instruments at the Electron Imaging Center for NanoMachines supported by NIH (1S10RR23057 and 1S10OD018111), NSF (DBI-1338135) and CNSI at UCLA.

346 **References**

347 1. J. A. Young, R. J. Collier, Anthrax toxin: receptor binding, internalization, pore formation, and
348 translocation. *Annu. Rev. Biochem.* **76**, 243-265 (2007).
349 2. K. L. Thoren, B. A. Krantz, The unfolding story of anthrax toxin translocation. *Molecular*
350 *microbiology* **80**, 588-595 (2011).
351 3. E. Santelli, L. A. Bankston, S. H. Leppia, R. C. Liddington, Crystal structure of a complex between
352 anthrax toxin and its host cell receptor. *Nature* **430**, 905 (2004).
353 4. A. F. Kintzer *et al.*, The protective antigen component of anthrax toxin forms functional
354 octameric complexes. *Journal of molecular biology* **392**, 614-629 (2009).
355 5. J. Mogridge, K. Cunningham, R. J. Collier, Stoichiometry of anthrax toxin complexes.
356 *Biochemistry* **41**, 1079-1082 (2002).
357 6. C. Antoni *et al.*, Cryo-EM structure of the fully-loaded asymmetric anthrax lethal toxin in its
358 heptameric pre-pore state. *bioRxiv* (2020).
359 7. L. Abrami, S. Liu, P. Cosson, S. H. Leppla, F. G. van der Goot, Anthrax toxin triggers endocytosis of
360 its receptor via a lipid raft–mediated clathrin-dependent process. *J Cell Biol* **160**, 321-328 (2003).
361 8. C. J. Miller, J. L. Elliott, R. J. Collier, Anthrax protective antigen: prepore-to-pore conversion.
362 *Biochemistry* **38**, 10432-10441 (1999).
363 9. B. A. Krantz, A. Finkelstein, R. J. Collier, Protein translocation through the anthrax toxin
364 transmembrane pore is driven by a proton gradient. *Journal of molecular biology* **355**, 968-979
365 (2006).
366 10. N. S. Duesbery *et al.*, Proteolytic inactivation of MAP-kinase-kinase by anthrax lethal factor.
367 *Science* **280**, 734-737 (1998).
368 11. G. K. Feld *et al.*, Structural basis for the unfolding of anthrax lethal factor by protective antigen
369 oligomers. *Nature structural & molecular biology* **17**, 1383-1390 (2010).
370 12. B. A. Krantz *et al.*, A phenylalanine clamp catalyzes protein translocation through the anthrax
371 toxin pore. *Science* **309**, 777-781 (2005).
372 13. J. Jiang, B. L. Pentelute, R. J. Collier, Z. H. Zhou, Atomic structure of anthrax PA pore elucidates
373 toxin translocation. *Nature* **521**, 545 (2015).
374 14. B. L. Pentelute, O. Sharma, R. J. Collier, Chemical dissection of protein translocation through the
375 anthrax toxin pore. *Angewandte Chemie International Edition* **50**, 2294-2296 (2011).
376 15. M. J. Brown, K. L. Thoren, B. A. Krantz, Role of the α clamp in the protein translocation
377 mechanism of anthrax toxin. *Journal of molecular biology* **427**, 3340-3349 (2015).
378 16. A. Machen *et al.*, Asymmetric cryo-EM structure of anthrax toxin protective antigen pore with
379 lethal factor N-terminal domain. *Toxins* **9**, 298 (2017).
380 17. N. J. Hardenbrook *et al.*, Atomic structures of anthrax toxin protective antigen channels bound
381 to partially unfolded lethal and edema factors. *Nature Communications* **11**, 1-10 (2020).
382 18. N. Akkaladevi *et al.*, Assembly of anthrax toxin pore: Lethal-factor complexes into lipid
383 nanodiscs. *Protein Science* **22**, 492-501 (2013).
384 19. N. Akkaladevi *et al.*, Following natures lead: on the construction of membrane-inserted toxins in
385 lipid bilayer nanodiscs. *The Journal of membrane biology* **248**, 595-607 (2015).
386 20. E. Gogol *et al.*, Three dimensional structure of the anthrax toxin translocon–lethal factor
387 complex by cryo-electron microscopy. *Protein Science* **22**, 586-594 (2013).
388 21. H. Katayama *et al.*, Three-dimensional structure of the anthrax toxin pore inserted into lipid
389 nanodiscs and lipid vesicles. *Proceedings of the National Academy of Sciences* **107**, 3453-3457
390 (2010).
391 22. P. Ma, A. E. Cardenas, M. I. Chaudhari, R. Elber, S. B. Rempe, The impact of protonation on early
392 translocation of anthrax lethal factor: Kinetics from molecular dynamics simulations and
393 milestoning theory. *Journal of the American Chemical Society* **139**, 14837-14840 (2017).

394 23. M. T. Fisher, S. Naik (2019) Systems and methods for identifying protein stabilizers. (Google
395 Patents).
396 24. T. H. Bayburt, S. G. Sligar, Membrane protein assembly into Nanodiscs. *FEBS letters* **584**, 1721-
397 1727 (2010).
398 25. I. Denisov, Y. Grinkova, A. Lazarides, S. Sligar, Directed self-assembly of monodisperse
399 phospholipid bilayer Nanodiscs with controlled size. *Journal of the American Chemical Society*
400 **126**, 3477-3487 (2004).
401 26. T. Ritchie *et al.*, Chapter eleven-reconstitution of membrane proteins in phospholipid bilayer
402 nanodiscs. *Methods in enzymology* **464**, 211-231 (2009).
403 27. B. A. Krantz, A. D. Trivedi, K. Cunningham, K. A. Christensen, R. J. Collier, Acid-induced unfolding
404 of the amino-terminal domains of the lethal and edema factors of anthrax toxin. *Journal of*
405 *molecular biology* **344**, 739-756 (2004).
406 28. F. Wruck *et al.*, The ribosome modulates folding inside the ribosomal exit tunnel. *BioRxiv*
407 (2020).
408 29. J. Sun, P. Jacquez, Roles of anthrax toxin receptor 2 in anthrax toxin membrane insertion and
409 pore formation. *Toxins* **8**, 34 (2016).
410 30. D. B. Lacy, D. J. Wigelsworth, R. A. Melnyk, S. C. Harrison, R. J. Collier, Structure of heptameric
411 protective antigen bound to an anthrax toxin receptor: a role for receptor in pH-dependent pore
412 formation. *Proceedings of the National Academy of Sciences of the United States of America* **101**,
413 13147-13151 (2004).
414 31. S. Zhang, A. Finkelstein, R. J. Collier, Evidence that translocation of anthrax toxin's lethal factor is
415 initiated by entry of its N terminus into the protective antigen channel. *Proceedings of the*
416 *National Academy of Sciences* **101**, 16756-16761 (2004).
417 32. P. Gupta, S. Singh, A. Tiwari, R. Bhat, R. Bhatnagar, Effect of pH on stability of anthrax lethal
418 factor: correlation between denaturation and activity. *Biochemical and biophysical research*
419 *communications* **284**, 568-573 (2001).
420 33. D. Das, B. A. Krantz, Peptide-and proton-driven allosteric clamps catalyze anthrax toxin
421 translocation across membranes. *Proceedings of the National Academy of Sciences* **113**, 9611-
422 9616 (2016).
423 34. D. Das, B. A. Krantz, Secondary Structure Preferences of the Anthrax Toxin Protective Antigen
424 Translocase. *Journal of molecular biology* **429**, 753-762 (2017).
425 35. L. Dmochewitz *et al.*, Role of CypA and Hsp90 in membrane translocation mediated by anthrax
426 protective antigen. *Cellular microbiology* **13**, 359-373 (2011).
427 36. D. N. Wilson, R. Beckmann, The ribosomal tunnel as a functional environment for nascent
428 polypeptide folding and translational stalling. *Current opinion in structural biology* **21**, 274-282
429 (2011).
430 37. O. Knapp *et al.*, Residues involved in the pore-forming activity of the C lostridium perfringens
431 iota toxin. *Cellular microbiology* **17**, 288-302 (2015).
432 38. T. Neumeyer *et al.*, Clostridium botulinum C2 Toxin IDENTIFICATION OF THE BINDING SITE FOR
433 CHLOROQUINE AND RELATED COMPOUNDS AND INFLUENCE OF THE BINDING SITE ON
434 PROPERTIES OF THE C2II CHANNEL. *Journal of Biological Chemistry* **283**, 3904-3914 (2008).
435 39. S. De, R. Olson, Crystal structure of the Vibrio cholerae cytolysin heptamer reveals common
436 features among disparate pore-forming toxins. *Proceedings of the National Academy of Sciences*
437 **108**, 7385-7390 (2011).
438 40. S. J. Piper *et al.*, Cryo-EM structures of the pore-forming A subunit from the Yersinia
439 entomophaga ABC toxin. *Nature communications* **10**, 1952 (2019).
440 41. T. Yamada *et al.*, Cryo-EM structures reveal translocational unfolding in the clostridial binary iota
441 toxin complex. *Nature structural & molecular biology* **27**, 288-296 (2020).

42. T. Sugawara *et al.*, Structural basis for pore-forming mechanism of staphylococcal α-hemolysin. *Toxicon* **108**, 226-231 (2015).
43. D. J. Wigelsworth *et al.*, Binding stoichiometry and kinetics of the interaction of a human anthrax toxin receptor, CMG2, with protective antigen. *Journal of Biological Chemistry* **279**, 23349-23356 (2004).
44. A. J. Machen *et al.*, Analyzing Dynamic Protein Complexes Assembled On and Released From Biolayer Interferometry Biosensor Using Mass Spectrometry and Electron Microscopy. *JoVE (Journal of Visualized Experiments)*, e57902 (2018).
45. D. N. Mastronarde, Automated electron microscope tomography using robust prediction of specimen movements. *Journal of structural biology* **152**, 36-51 (2005).
46. A. Punjani, J. L. Rubinstein, D. J. Fleet, M. A. Brubaker, cryoSPARC: algorithms for rapid unsupervised cryo-EM structure determination. *Nature Methods* **14**, 290-296 (2017).
47. S. Q. Zheng *et al.*, MotionCor2: anisotropic correction of beam-induced motion for improved cryo-electron microscopy. *Nature methods* **14**, 331-332 (2017).
48. T. C. Terwilliger, S. J. Ludtke, R. J. Read, P. D. Adams, P. V. Afonine, Improvement of cryo-EM maps by density modification. *Nature Methods* **17**, 923-927 (2020).
49. P. D. Adams *et al.*, PHENIX: a comprehensive Python-based system for macromolecular structure solution. *Acta Crystallographica Section D: Biological Crystallography* **66**, 213-221 (2010).
50. E. F. Pettersen *et al.*, UCSF Chimera—a visualization system for exploratory research and analysis. *Journal of computational chemistry* **25**, 1605-1612 (2004).
51. P. Emsley, K. Cowtan, Coot: model-building tools for molecular graphics. *Acta Crystallographica Section D: Biological Crystallography* **60**, 2126-2132 (2004).
52. V. B. Chen *et al.*, MolProbity: all-atom structure validation for macromolecular crystallography. *Acta Crystallographica Section D: Biological Crystallography* **66**, 12-21 (2010).

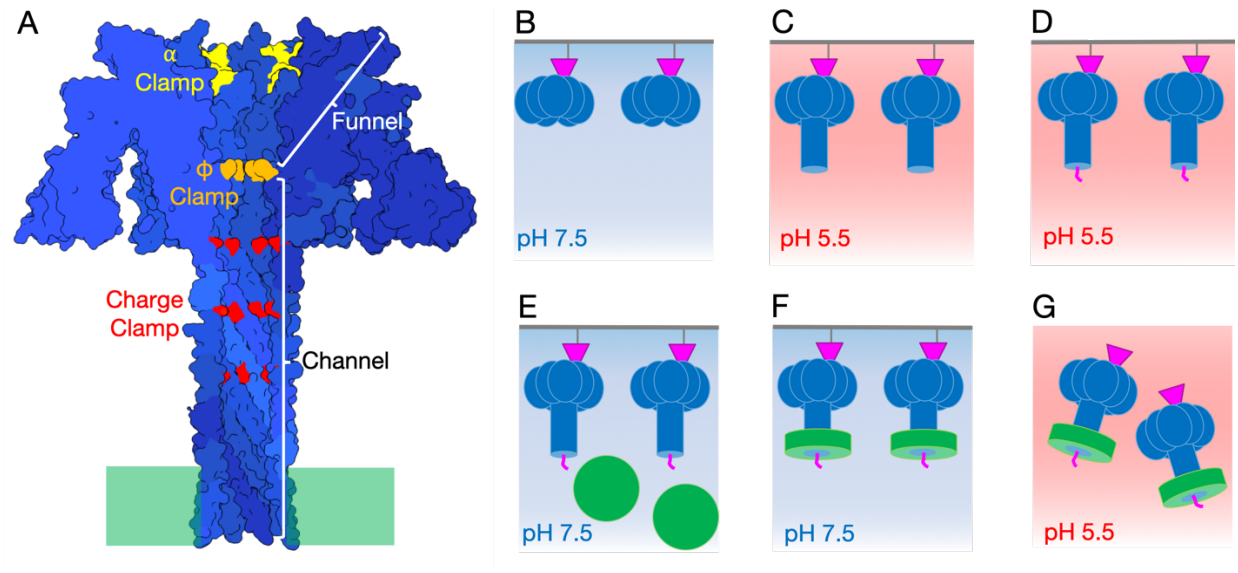

468

469 **Fig. 1. Anthrax toxin immobilization, translocation, and nanodisc stabilization (TITaNS)**

470 **method** (A) PA_{pore} side view slice with funnel shape from α clamp (yellow) to Φ clamp (orange)

471 and charge clamp (red) inside pore β barrel channel indicated. (B) Immobilization of LF_N

472 (magenta) $PA_{prepore}$ (blue) complexes on thiol sepharose beads (grey surface). (C) $PA_{prepore}$

473 transitioned to PA_{pore}. (D) Predicted translocation complex of LF_N -PA_{pore} at low pH. (E) Addition

474 of pre-nanodisc micelle (green) to complex. (F) Nanodisc formation. (G) LF_N-PA_{pore}-Nanodisc

475 translocation complexes at pH 5.5 on cryoEM grid.

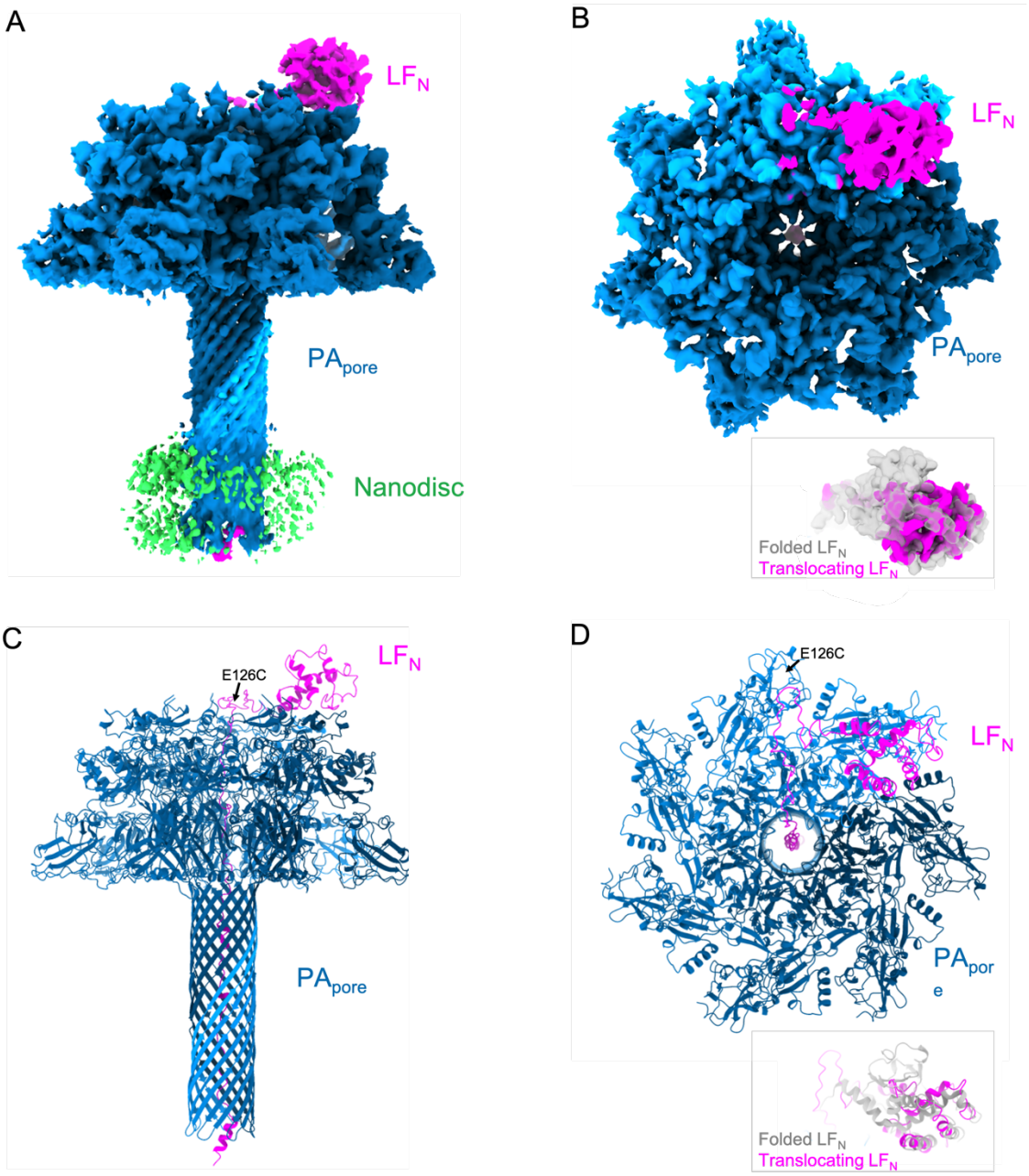

476

477 **Fig. 2. Overview of the anthrax toxin translocation complex.** CryoEM density map (A) side
478 and (B) top view of LF_N translocating through PA_{pore}. Inset: folded LF_N model density (PDB 6PSN)
479 compared to translocating LF_N density. Molecular model (C) side and (D) top view of LF_N
480 translocating through PA_{pore}. Inset: folded LF_N model (PDB 6PSN) compared to translocating LF_N
481 model.

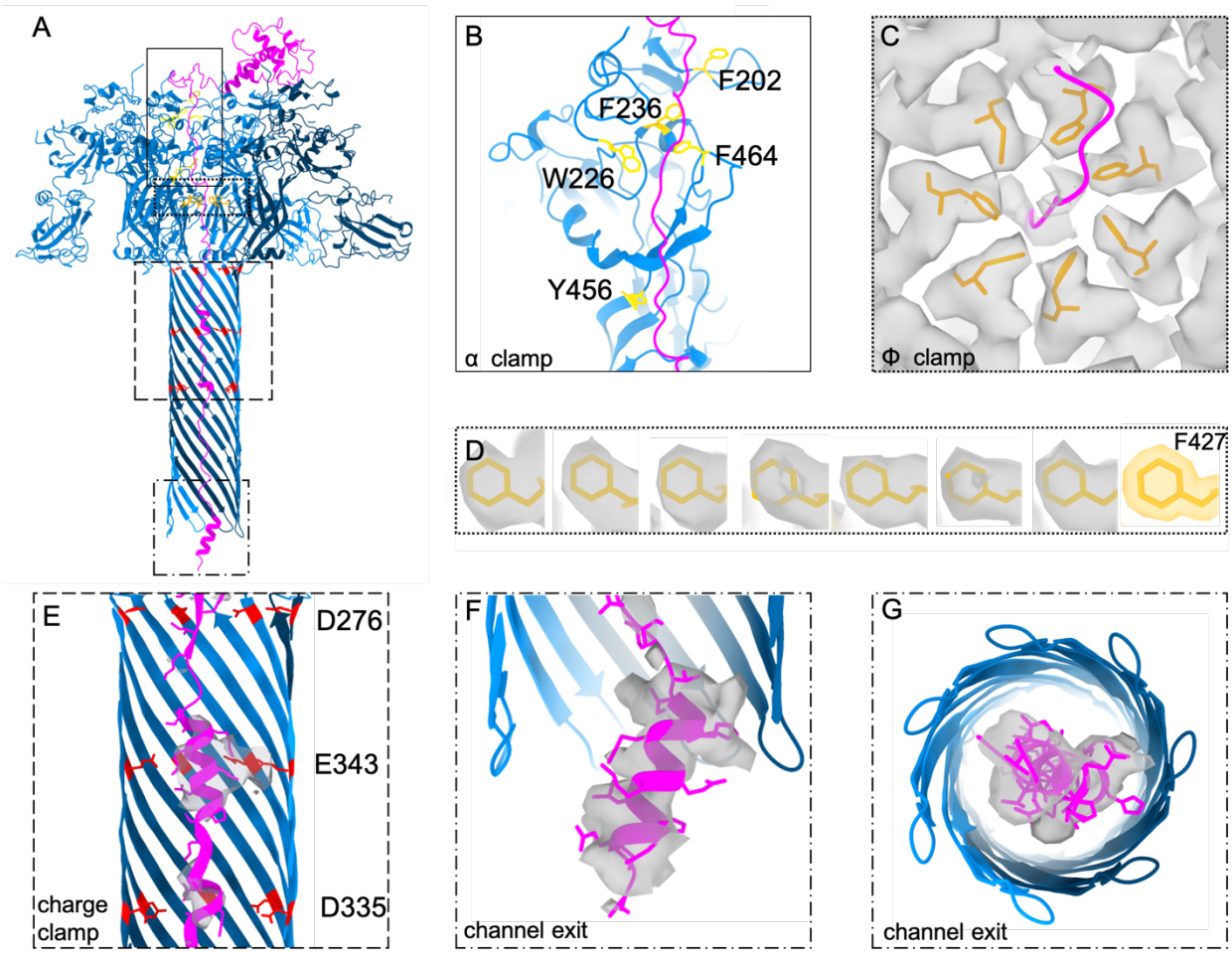

Figure 3. Unfolding and refolding of LF_N at key clamp sites during translocation through PA_{pore}. (A) Model of PA_{pore} (blue) translocating LF_N (magenta) with α clamp, Φ clamp, and charge clamp residues shown in yellow, orange, and red respectively. (B) Hydrophobic residues predicted to facilitate unfolding in early translocation from α clamp to Φ clamp. (C) Φ clamp ring with LF_N density. (D) Individual F427 residues (orange) with associated cryo-EM density (grey) for each subunit compared to modelled density (orange). (E) LF_N model (magenta) and density (grey) in β barrel charge clamp (F) PA_{pore} channel exit into the cytosol with LF_N α1 helical model (magenta) and density (grey). (G) 90° rotation of F.

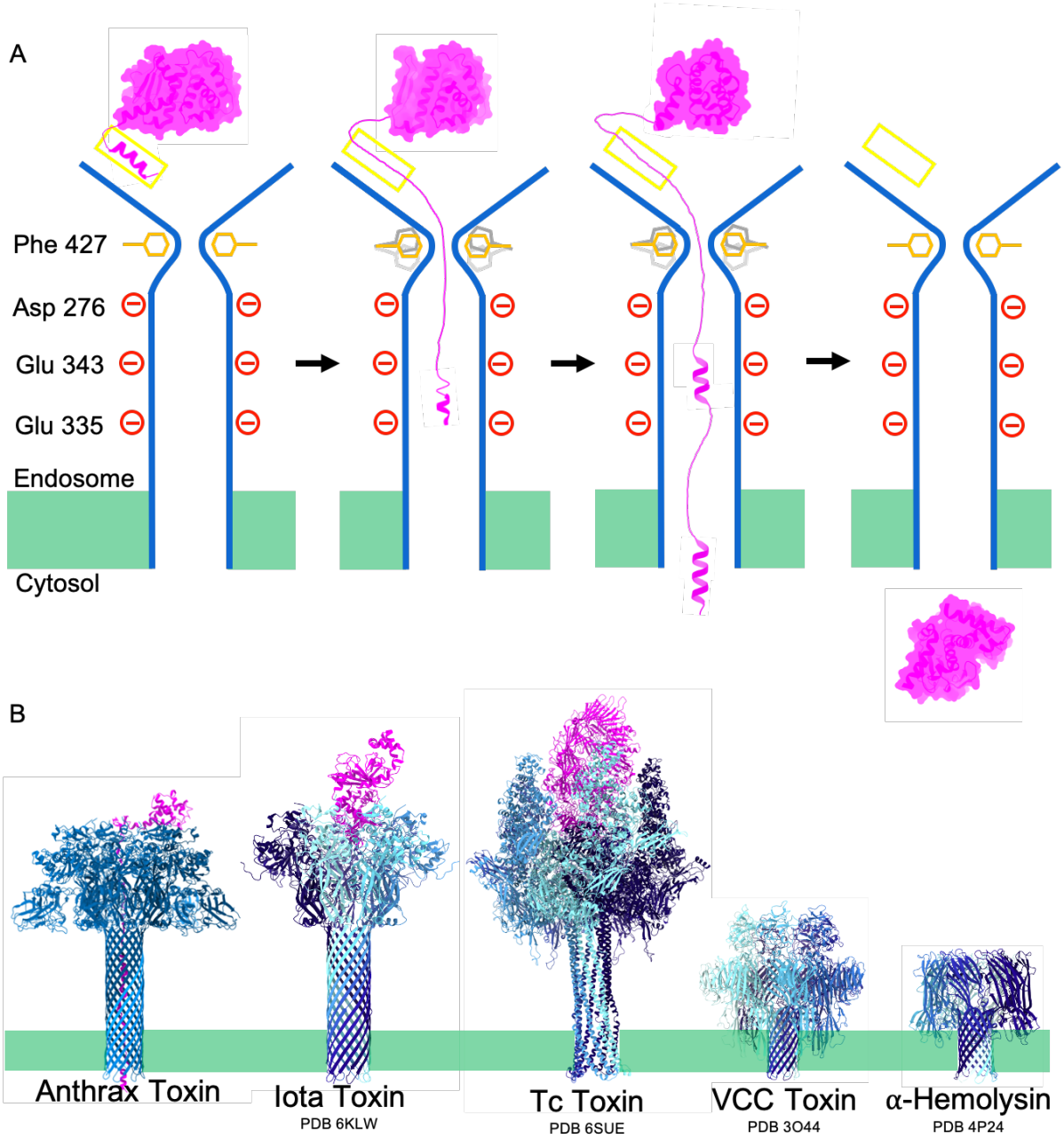

Fig. 4. Proposed AB toxin extended pore refolding mechanism. (A) Unfolding-refolding translocation model of anthrax toxin. LF_N (magenta) translocates through PA_{pore} (blue) passing the α clamp (yellow), the Φ clamp (orange and grey), and the charge clamp (red). Helical portions of LF_N begin to refold in the channel ensuring proper tertiary refolding of LF_N. (B) Comparison of toxin pore length between toxins that translocate proteins vs toxins that disrupt ion gradients. Membrane bilayer represented in green.

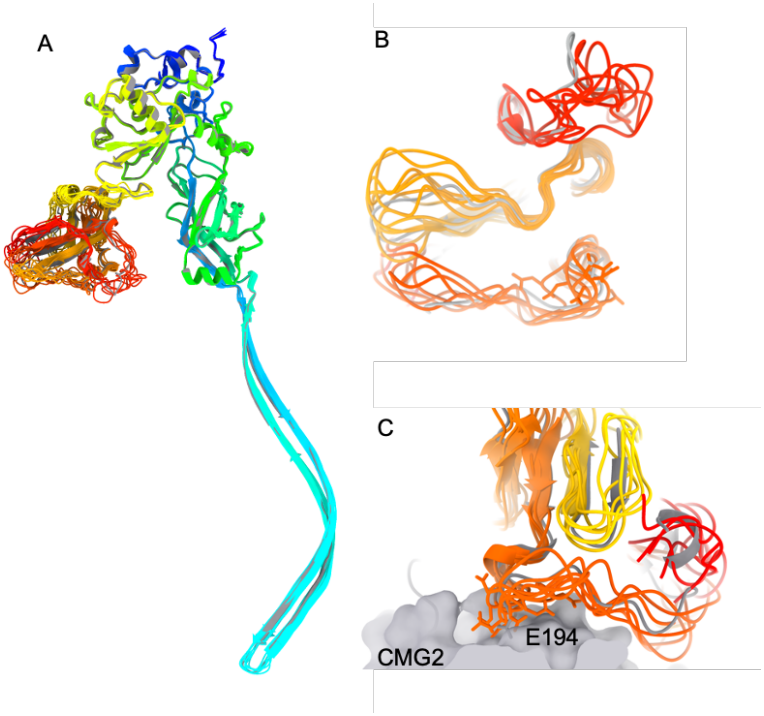

Fig. S1. Comparison of PA_{pore} protomers. (A) PA_{pore} protomer chains are shown in rainbow N to C termini for chains A-G. The receptor binding domain is shown in yellow, red, and orange. (B) Bottom up view of receptor binding domain with $PA_{prepore}$ receptor binding domain shown in grey (PDB 1T6B). (C) Comparison of PA_{pore} protomers to $PA_{prepore}$ bound to receptor CMG2 (grey).

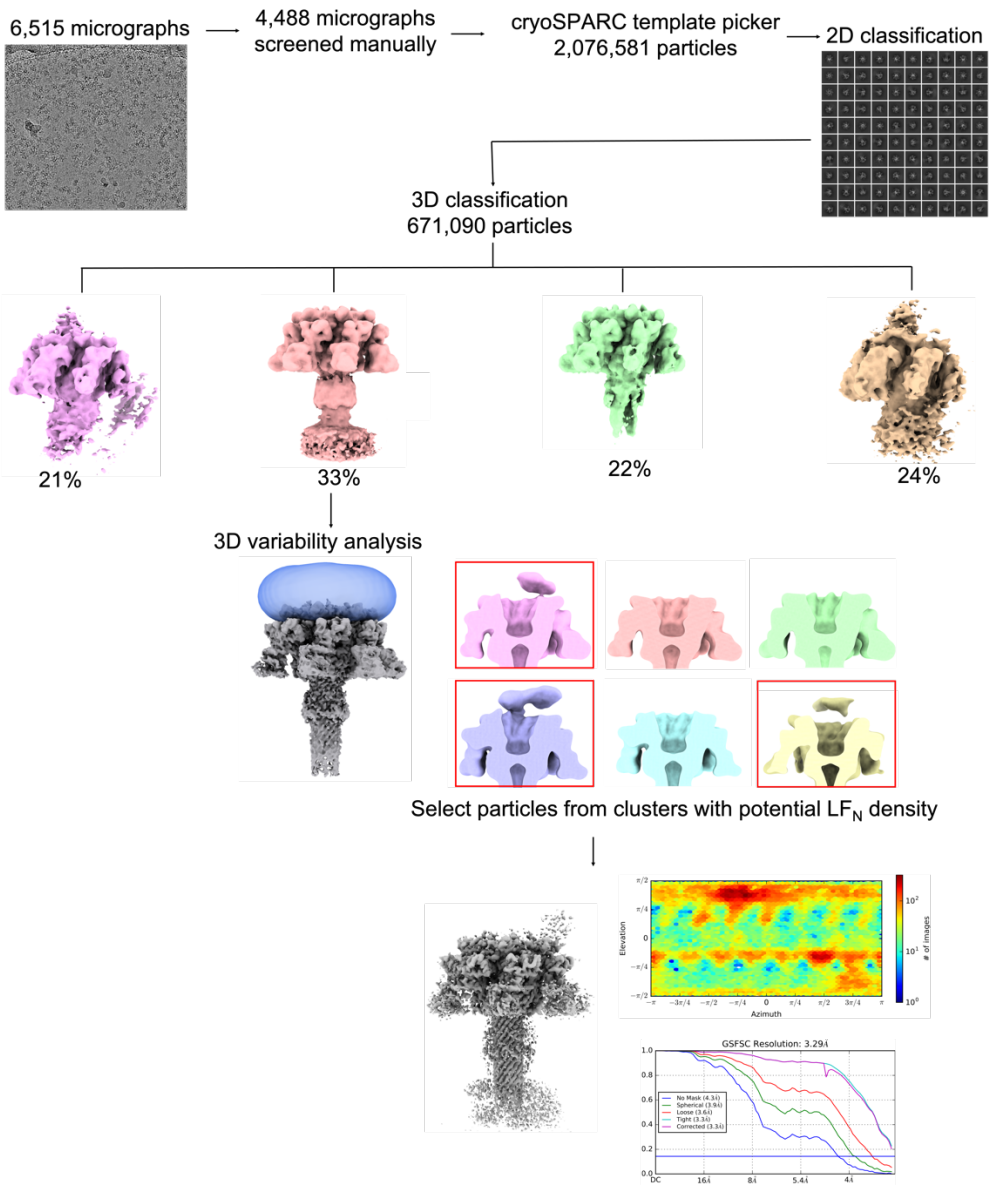

Fig. S2. Single particle analysis of anthrax toxin translocating complexes. After micrograph curation and 2D classification, 'good' particles were subjected to 3D classification (four classes) followed by 3D variability analysis on particles that contained intact β barrel. 3D variability analysis focused on potential LF_N binding sites (blue mask) above PA_{pore} (grey). Results of 3D variability analysis are shown in pastels filtered to 20 Å (pink, orange, green, purple, blue, yellow) with potential LF_N density containing maps boxed in red. 3.3 Å Non-uniform refinement of PA_{pore} with intact β barrel and potential LF_N density is shown in grey (FSC cutoff 0.143). Euler angle distribution of particles shows diverse particle orientations.

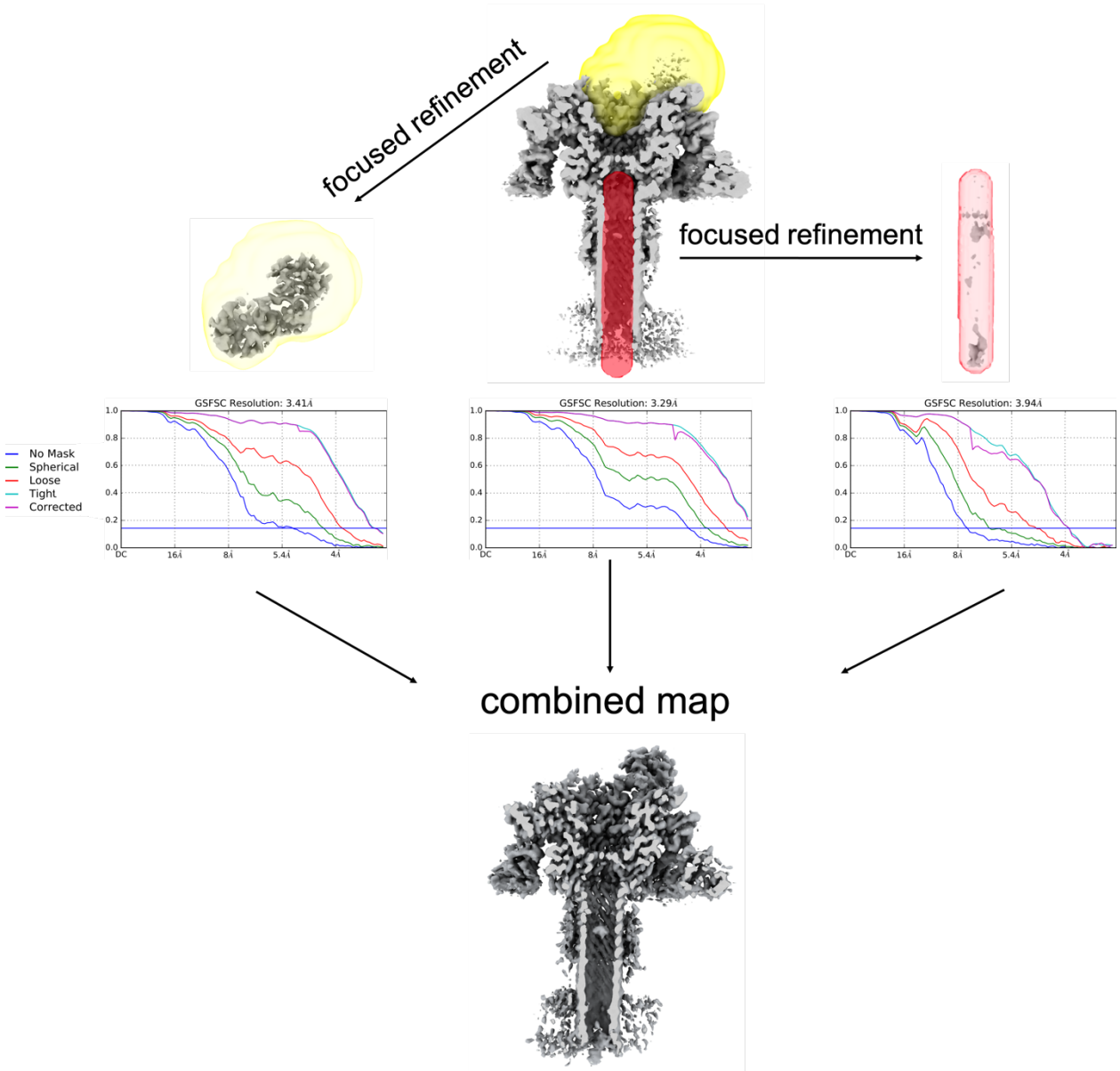

Fig. S3. Density modification of cryoEM map. Focused refinement and density modification of non-uniform refined cryoEM map were perfomed in cryoSPARC and Phenix, respectively. Density for LF_N above PA_{pore}, PA_{pore}, and β barrel interior were combined using Phenix combine focus maps. Resolution was determined for each density prior to combining using FSC cutoff of 0.143.

518 **Table S1. cryoEM Data Collection and Processing Statistics**

Data collection and processing	
Magnification	130,000X
Voltage (kV)	300
Electron exposure (e^{-}/Å^{2})	1.79 per frame
Defocus range (μm)	1-3um
Pixel size (Å)	0.535
Symmetry imposed	C1
Initial particle images (no.)	2076581
Final particle images (no.)	122651
Map resolution (Å)	3.3
FSC threshold	0.143
Refinement	
Initial model used (PDB ID)	6PSN
Model resolution (Å)	3.3
FSC threshold	0.143
Model composition	
Nonhydrogen atoms	32826
Protein residues	4154
Ligands	14
B factors (Å^{2})	
Protein	395
Ligand	202
r.m.s. deviations	
Bond Length (Å) (# > 4σ)	0.009 (2)
Bond Angles (°) (# > 4σ)	1.311 (37)
Validation	
MolProbity score	2.75
Clashscore	26
Poor rotamers (%)	4.1
Ramachandran plot	
Favored (%)	94.25
Allowed (%)	5.32
Disallowed (%)	0.43

519